

Luminescence analysis of charge carrier separation and internal series resistance losses in Cu(In,Ga)Se₂ solar cells

Uwe Rau, Vito Huhn, and Bart E. Pieters
IEK5-Photovoltaik, Forschungszentrum Jülich, 52425 Jülich, Germany

Abstract

Cu(In,Ga)Se₂ solar cells are investigated by luminescence measurements. We construct the current vs. internal voltage characteristics of these devices from the luminescence intensity at different voltage and light bias conditions. A comparison of these characteristics to electrically measured current vs. voltage curves unveils an internal resistance loss that is strongly dependent on voltage bias and illumination. Especially, we find significant residual luminescence for the device under short circuit conditions. Numerical device simulations reveal that this effect is caused by a drop of the electron Quasi-Fermi-level within the space charge region of the absorber material. We use a modified equivalent circuit model to describe the observed behavior in terms of simple equations. We show that such a voltage dependent series resistance leads to a violation of a linear network theorem which under standard circumstances provides a useful method for the determination of the photocurrent collection efficiency. An analysis of resistive and recombination losses in the devices demonstrates that the internal voltage dependent series resistance causes an efficiency loss of about 1.3 % (absolute) for a device with an efficiency 13.4 %. Finally, we show that the observed behavior is general feature of charge carrier separation in solar cells with finite charge carrier mobility and that the intensity of the residual short circuit luminescence provides valuable information on the efficiency of this process.

I. Introduction

The collection of the photogenerated charge carriers, electrons and holes, at two different contacts lies in the heart of the photovoltaic action of any solar cell. Perfect carrier collection implies that every electron hole pair contributes to the short circuit current. This in turn, is only possible if under short circuit conditions the concentration of excess carriers in the solar cell is virtually zero because otherwise some of the charge carriers will be lost by radiative recombination.[1] Thus, in a perfect solar cell as described in the Shockley-Queisser model [2] we can switch off any luminescence by putting the terminal voltage of an illuminated solar cell to zero. Inversely, the detection of photoluminescence from a solar cell under short circuit conditions is directly indicative for a departure from the ideal case and, consequently, for an efficiency loss. Electro- and photoluminescence analysis [3,4,5,6,7,8,9] of solar cells is based on the intimate connection between luminescent and photovoltaic materials properties as expressed by the opto-electronic reciprocity theorem [10] and by the generalized Plank's law.[11] In most cases, luminescence experiments are conducted either under voltage bias (electroluminescence) or by using uncontacted samples, which corresponds to open circuit conditions (photoluminescence). For crystalline silicon solar cells, photoluminescence under short circuit conditions was reported by Abbott et al. [12] as well as by Hinken and co-workers [13] who determined the effective diffusion length in crystalline Si solar cells from the difference between photoluminescence under open circuit and that under short circuit conditions. Juhl and Trupke [14] discussed the luminescence generated by 'voltage independent charge carriers' in the context of implied open circuit voltages determined by photoluminescence measurements. Finally, it was shown that the luminescence of a solar cell is the superposition of a contribution driven by the external voltage and the luminescence under short circuit. [15]

The present paper investigates the photoluminescence of industrially produced Cu(In,Ga)Se₂ solar cells under variations of the external voltage bias down to short circuit conditions. Like in the case of crystalline Si solar cells, we find a significant luminescence intensity under short circuit. However, in the Si solar cells this residual luminescence stems from diffusion limitations in the very thick quasi-neutral zone of the absorber [12,13,14] whereas in the present Cu(In,Ga)Se₂ solar cells the luminescence is a result of an *internal* series resistance across the space charge region (SCR) of the device. The investigation of an internal series resistance goes beyond earlier investigations that were restricted to *external* series resistance effects, like the sheet resistance of the emitter of silicon wafer solar cells [16,17,18] or window layers of thin film solar cells.[19,20,21,22]

The internal series resistance in the Cu(In,Ga)Se₂ solar cells under investigation turns out to be strongly dependent on voltage bias. Note that effects from an internal series resistance have been investigated earlier by experiments on *pin*-cells solar cells made from microcrystalline Si [23] and from organic semiconductors [24]. In contrast to these models based on a *pin*-type device structure, the present results are explained in terms of the *pn*-type junction present in the Cu(In,Ga)Se₂ solar cell. For an analytical expression describing this behavior we solve the drift-diffusion equation for minority carriers in the SCR of the cell under light and/or voltage bias. This solution turns out to be compatible with an equivalent circuit model for the solar cell recently introduced by Breitenstein [25,26]. Our experimental results agree well with the theoretical description by the equivalent circuit model as well with more detailed numerical simulations. We finally discuss the importance of our findings in view of the general mechanisms of charge carrier collection in solar cells and, especially, with respect

to the network theorem of Wong and Green [27] that is the basis of the photocurrent collection method for the analysis of resistive and recombination losses in solar cells [28, 29, 30, 31, 32].

II. Theory

A. Quasi-Fermi levels in the space charge region

Figure 1 shows the band diagram of a ZnO/CdS/Cu(In,Ga)Se₂ heterojunction solar cell under illumination and at external short circuit. It is clearly visible that a considerable split between the electron Quasi-Fermilevel (QFL) E_{Fn} and the hole QFL E_{Fp} exists in the SCR as well as in the neutral region of the device. Therefore, also the concentrations n of electrons and the concentration p of holes deviate considerably from their equilibrium values n_0 and p_0 , respectively. In the bulk of the device up to half way through the SCR, we have $E_{Fn} > 0$ and for the second half of the SCR and beyond $E_{Fp} < 0$. In the following we derive an analytical solution for the minority carrier (electron) QFL through the SCR under light and/or voltage bias.

The electron current density J_n in the SCR is assumed to be constant. The electron current density is defined by the concentration of electrons and the gradient of the electron QFL according to [33]

$$J_n = -\mu_n n(z) \frac{dE_{Fn}(z)}{dz} = -\mu_n N_C \exp\left(\frac{E_{Fn}(z) - E_C(z)}{kT}\right) \frac{dE_{Fn}(z)}{dz} \quad (1)$$

where μ_n denotes the electron mobility, N_C the effective density of states in the conduction band, E_C the energy of the conduction band, and kT the thermal energy. With constant J_n and a given dependence of the conduction band energy on the spatial coordinate z , Eq. (1) is a differential equation for E_{Fn} . Let us assume that the zero of the coordinate system (for energy

E and coordinate z) is at the edge of the SCR such that in the depletion approximation the energy of the conduction band follows

$$E_C(z) = E_C(0) - \frac{q^2 N_A}{2\epsilon_s} z^2 = E_C(0) - az^2. \quad (2)$$

With this approximation we find that the solution of Eq. (1) is given by

$$E_{Fn}(z) = kT \log \left(\exp \left\{ \frac{E_{Fn}(0)}{kT} \right\} - \frac{J_n}{2\mu_n N_C kT} \exp \left\{ \frac{E_C(0)}{kT} \right\} \frac{\sqrt{\pi} \operatorname{erf} \left\{ z \sqrt{a/kT} \right\}}{\sqrt{a/kT}} \right). \quad (3)$$

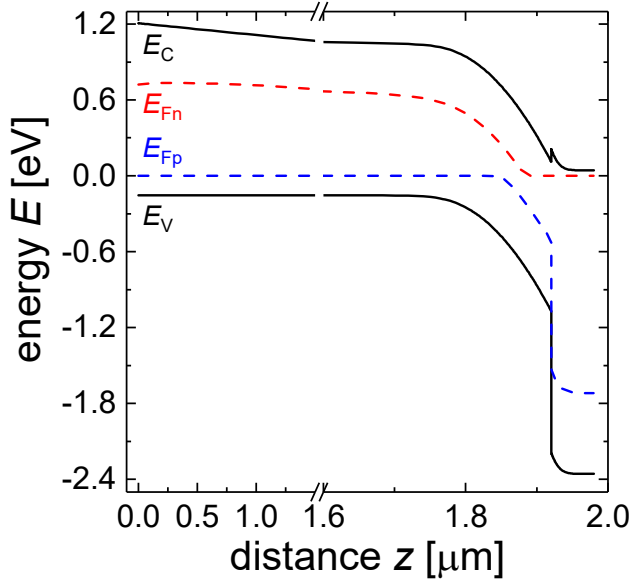


Fig. 1: Band diagram of a graded CdS/Cu(In,Ga)Se₂ heterojunction solar cell under external short circuit and under illumination from the right hand side, as calculated numerically (SCAPS). The significant split of the quasi-Fermi-levels E_{Fn} and E_{Fp} of electrons and holes in the Cu(In,Ga)Se₂ absorber is clearly visible. The Cu(In,Ga)Se₂ absorber has a significant Ga-grading towards the back contact (left) leading to a gradient in the conduction band energy E_c .

Resolving Eq. (3) for the electron current density and for the boundary conditions at $z = 0$ and $z = w$ yields

$$J_n = \mu_n N_C kT \exp\left\{\frac{-E_C(0)}{kT}\right\} \frac{2\sqrt{a/kT}}{\sqrt{\pi} \operatorname{erf}\{w\sqrt{a/kT}\}} \left(\exp\left\{\frac{E_{Fn}(0)}{kT}\right\} - \exp\left\{\frac{E_{Fn}(w)}{kT}\right\} \right) \quad (4)$$

where w denotes the width of the SCR. With Eq. (4) the current through the SCR is determined by the values of the electron QFL at the two edges of the SCR. As shown in Fig. 2, we use the equilibrium Fermi energy E_F^0 to define the external voltage via $qV_{ext} = E_{Fn}(w) - E_F^0$.

Accordingly, we replace the electron QFL $E_{Fn}(0)$ by an internal voltage $qV_{int} = E_{Fn}(0) - E_F^0$.

With this Eq. (4) becomes

$$J_n = \mu_n N_C kT \exp\left\{\frac{E_F^0 - E_C(0)}{kT}\right\} \frac{2\sqrt{a/kT}}{\sqrt{\pi} \operatorname{erf}\{w\sqrt{a/kT}\}} \left(\exp\left\{\frac{qV_{int}}{kT}\right\} - \exp\left\{\frac{qV_{ext}}{kT}\right\} \right). \quad (5)$$

Because of $qV_{bi} = aw^2$, the argument of the error function (erf) in Eq. (5) may be expressed via the built-in potential V_{bi} , i.e. $w\sqrt{a/kT} = qV_{bi}/kT$. Likewise, we may use the Debye length

$L_D = (\epsilon_s kT / q^2 N_A)^{1/2} = (kT / 2a)^{1/2}$ [33] to write

$$J_n = \sigma_n^0 \frac{kT}{q} \frac{\sqrt{2}/L_D}{\sqrt{\pi} \operatorname{erf}\{w/\sqrt{2}L_D\}} \left(\exp\left\{\frac{qV_{int}}{kT}\right\} - \exp\left\{\frac{qV_{ext}}{kT}\right\} \right) \quad (6)$$

using the equilibrium conductivity σ_n^0 for electrons in the neutral region. If we have $V_{bi} \gg 2kT/q$ or $w \gg 3L_D$ the error function approaches unity and Eq. (6) simplifies to

$$\begin{aligned} J_n &\approx \sigma_n^0 \sqrt{\frac{2}{\pi}} \frac{kT/q}{L_D} \left(\exp\left\{\frac{qV_{\text{int}}}{kT}\right\} - \exp\left\{\frac{qV_{\text{ext}}}{kT}\right\} \right) \\ &= J_B \left(\exp\left\{\frac{qV_{\text{ext}}}{kT}\right\} - \exp\left\{\frac{qV_{\text{int}}}{kT}\right\} \right) \end{aligned} \quad (7)$$

with a prefactor J_B in the second line that is independent of the internal and external voltage. Note that Eq. (7) corresponds to Eq. (2) derived by Breitenstein in Ref. [26] by a more phenomenological approach. We emphasize that Eq. (7) connects the two basic functionalities of a semiconductor junction in a solar cell: (i) the building of an external electrostatic potential V_{ext} as a result of the photo-generated non-equilibrium chemical potential of the charge carriers (expressed by the internal voltage V_{int}) and (ii) the loss of free energy during the collection of these free carriers. Furthermore, the current density J_n cannot be expressed as a function of the difference between V_{ext} and V_{int} . Rather J_n depends on a reference energy for both potentials, the equilibrium Fermi-level. One possibility to handle this issue within an equivalent circuit model is to define a resistance that is dependent on one of the two voltages (see Fig. 2b) as proposed by Breitenstein [25,26].

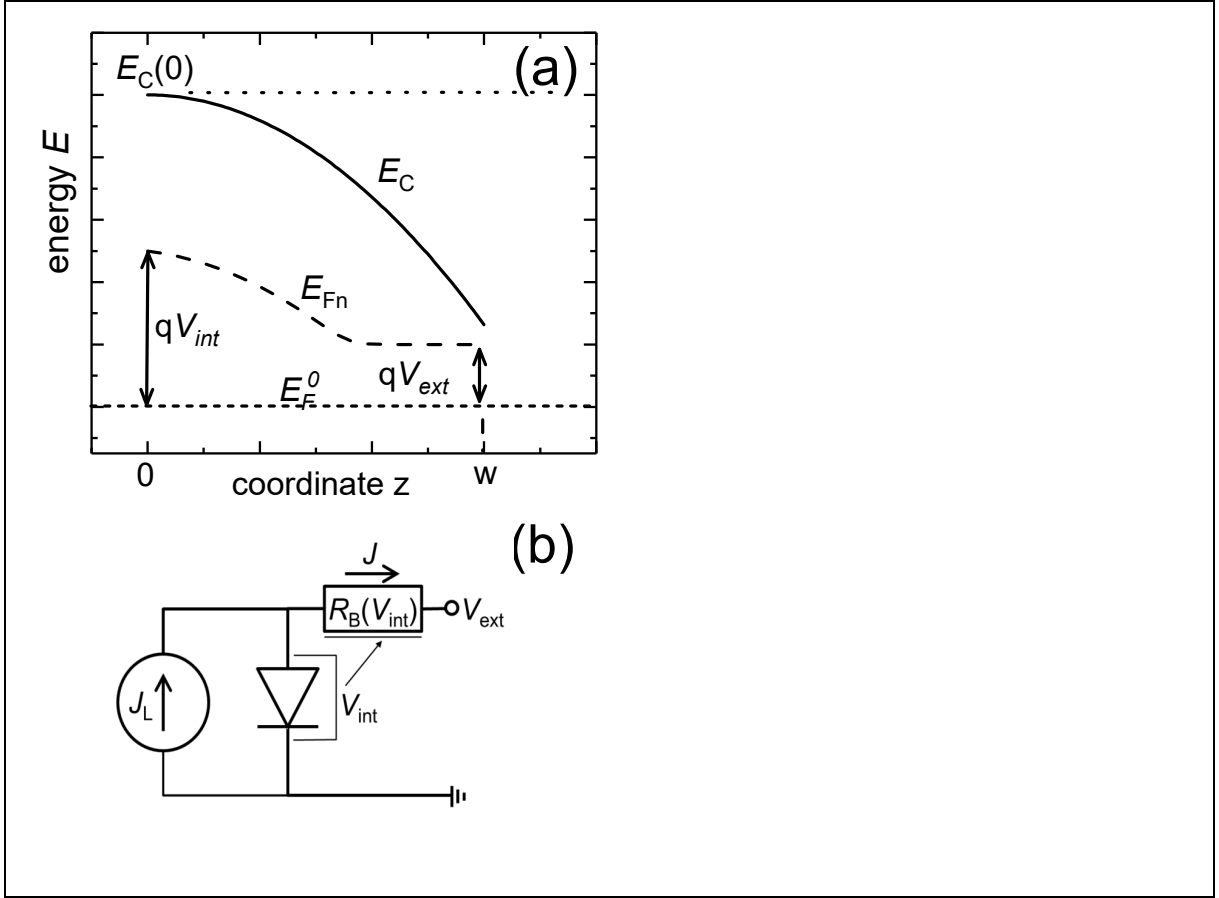


Fig. 2: (a) Definitions underlying the calculation of the electron quasi-Fermi-level E_{Fn} through the space charge region (SCR) of a pn-junction with width w and with a parabolic shape of the conduction band energy E_C . The internal voltage V_{int} is defined as the difference $qV_{int} = E_{Fn}(0) - E_F^0$ between the electron quasi-Fermi-level $E_{Fn}(0)$ at the edge of the SCR ($z = 0$). The external voltage is defined via $qV_{ext} = E_{Fn}(w) - E_F^0$. (b) The internal series resistance of the SCR resulting from the shape of $E_{Fn}(z)$ depends on the internal voltage V_{int} as described by a modified equivalent circuit model [25,26].

B. Internal series resistance and residual short circuit luminescence

The equivalent circuit shown in Fig. 2b contains a voltage dependent series resistance $R_B(V_{int})$ in addition to the usual current source for the photo-generated current density J_L and the recombination diode with the diode ideality factor n_{id} and a saturation current density J_0 . By setting the collected current density J_n equal to the internal recombination current density we obtain

$$J_B \left[\exp\left(\frac{qV_{\text{int}}}{kT}\right) - \exp\left(\frac{qV_{\text{ext}}}{kT}\right) \right] = J_L - J_0 \left[\exp\left(\frac{qV_{\text{int}}}{n_{id}kT}\right) - 1 \right]. \quad (8)$$

An analytical treatment of Eq. (8) is possible if the ideality factor on the right hand side is $n_{id} = 1$. Then, resolving Eq. (8) for the internal voltage yields the dependency of the internal on the external voltage yields

$$V_{\text{int}} = \frac{kT}{q} \log \left[\frac{J_B}{J_B + J_0} \exp\left(\frac{qV_{\text{ext}}}{kT}\right) + \frac{J_L + J_0}{J_B + J_0} \right]. \quad (9)$$

Equation (9) predicts for $V_{\text{ext}} = 0$ a residual short-circuit value for the internal voltage

$$V_{\text{int}}^{\text{SC}} = \frac{kT}{q} \log \left[\frac{J_B + J_L + J_0}{J_B + J_0} \right]. \quad (10)$$

Substituting V_{int} in Eq (8) by Eq. (9) yields for the current voltage (JV) curve of the entire equivalent circuit

$$\begin{aligned} J &= J_L - J_0 \left[\exp\left(\frac{qV_{\text{int}}}{kT}\right) - 1 \right] \\ &= \frac{J_B}{J_0 + J_B} \left\{ J_L - J_0 \left[\exp\left(\frac{qV_{\text{ext}}}{kT}\right) - 1 \right] \right\}, \end{aligned} \quad (11)$$

i.e., the $J(V_{\text{ext}})$ curve is a compressed version of the $J(V_{\text{int}})$ curve. This implies that the short circuit current density J_{SC} is reduced with respect to the photogenerated current density J_L by a factor $J_B / (J_0 + J_B)$. Note that with $J_L \gg J_0$ the present Eqs. (9) and (11) correspond to Eqs. (9) and (10) in Ref. [25].

The internal series resistance R_B can be finally expressed either as a function of the internal voltage or the external voltage via

$$\begin{aligned}
R_B &:= \frac{V_{\text{int}} - V_{\text{ext}}}{J} = \frac{V_{\text{int}} - \frac{kT}{q} \log \left\{ \frac{J_B + J_0}{J_B} \exp \left(\frac{qV_{\text{int}}}{kT} \right) - \frac{J_L + J_0}{J_B} \right\}}{J_L - J_0 \left\{ \exp \left(\frac{qV_{\text{int}}}{kT} \right) - 1 \right\}} \\
&= \frac{J_B + J_0}{J_0} \frac{\frac{kT}{q} \log \left\{ \frac{J_B}{J_B + J_0} \exp \left(\frac{qV_{\text{ext}}}{kT} \right) + \frac{J_L + J_0}{J_B + J_0} \right\} - V_{\text{ext}}}{J_L - J_0 \left\{ \exp \left(\frac{qV_{\text{ext}}}{kT} \right) - 1 \right\}}.
\end{aligned} \tag{12}$$

We note that the dependence of the internal series resistance on the internal voltage V_{int} as derived here for a *pn*-junction is different from the results obtained earlier for *pin*-junctions [23,24] which reads

$$R_{\text{int}} = R_0 \exp \left(\frac{-qV_{\text{int}}}{kT} \right). \tag{13}$$

In the following we will compare our experimental results with both approaches, i.e. the here derived model in Eq (12) and the *pin*-model in Eq (13).

III. Experimental Results and Discussion

A. Experimental set-up and numerical simulation method

For our experiments, we use industrially prepared ZnO/CdS/Cu(In,Ga)Se₂ solar cells prepared by co-evaporation [34]. The cells of size 1.6×0.4 cm² are positioned on 10 x 10 cm² large substrate which was cut from industrially produced modules. The cells were mounted into a luminescence imaging set-up as described in Refs. [31,32] that allows the homogeneous irradiation of the sample with a 808 nm laser. The laser intensity is adjusted such that the short circuit current density of the sample closely matches its short circuit current density under AM 1.5 G conditions (at AM 1.5 G: $J_{\text{SC}}^{\text{AM1.5}} = 29.2 \text{ mA/cm}^2$; at PL Setup: $J_{\text{SC}}^{\text{PLsetup}} = 30.98 \text{ mA/cm}^2$).

In Table 1 we summarize the solar cell properties as measured under various conditions. Within the setup current-voltage (IV) characteristics are measured in the dark and under illumination while simultaneously taking luminescence images. The only correction applied to the images

was a subtraction of a background image where the applied voltage to the sample was zero and the illumination was turned off.

Table 1: Solar cell parameters under various conditions. In the table the solar cell parameters under AM.15 G spectrum, 808 nm monochromatic laser light and 808 nm laser light corrected to the AM1.5 G short circuit current density. Note that the efficiency under 808 nm (*) is computed assuming an incoming power of a 1000 W/m², such that the value can be compared to the AM1.5 G spectrum value.

	J_{sc} [mA/cm ²]	V_{oc} [V]	FF [%]	η [%]
AM 1.5 G	29.2	0.713	65	13.5
808 nm	31.0	0.710	64	14.0*
808 nm corrected	29.2	0.710	64	13.4

For the numerical simulations we use the numerical device simulator SCAPS [35] which is especially suited to describe solar cells based on Cu(In,Ga)Se₂. The set of material parameters entering in our simulations is based on that used in Refs. [36,37]. We adapted this parameter set to our actual device (e.g. by including a heavy Ga-grading) and to fit our experimental results. These modifications are documented in the supplementary information to the present paper.

B. Luminescence results

Figure 3a-d shows a series of luminescence pictures of a Cu(In,Ga)Se₂ solar cell and illumination and at different external voltages. The signal of these pictures is then integrated over the entire cell area to yield a single value for the luminescence per picture. From this signal S_{em} the internal voltage V_{int} is determined with

$$V_{int} = \frac{kT}{q} \log(S_{em}) + V_{offs} . \quad (14)$$

We eliminate the unknown offset voltage V_{offs} (which is the same for all pictures) by scaling the value at open circuit in a way that $V_{int,OC} = V_{ext,OC}$ [38]. Herewith, we obtain the absolute values for V_{int} under all external bias conditions as depicted by the $V_{int}(V_{ext})$ curve in Fig.4. Since the current through the device is externally measured for each bias point we are able to deduce a current vs. internal voltage $J(V_{int})$ curve of the device as shown in Fig. 3e.

Figure 3e shows the JV -characteristics measured in the dark and under illumination ($J_{SC}^{lum} = 31.0 \text{ mAcm}^{-2}$). Also shown are both current vs. internal voltage $J(V_{int})$ curves. With respect to the externally measured curves, the dark $J(V_{int})$ curve is shifted towards higher voltages and the illuminated $J(V_{int})$ towards lower voltages. From the difference $V_{ext} - V_{int}$ at a given current density J the total series resistance as determined from the experiment is calculated via

$$R_S = \frac{V_{ext} - V_{int}}{J}. \quad (15)$$

Figure 5 displays the dependence of the series resistance R_S for the dark and the illuminated case on the external (5a) and on the internal voltage (5b).

C. Comparison to model and device simulations

In the following, we will compare our experimental results to the model outlined in section II where we use a numerical solution of Eq. (8) for the case of non-ideal recombination ($n_{id} \neq 1$). In a next step we perform numerical device simulations using SCAPS with the parameter set given in the supplementary information. The aim of the fitting procedure was to reproduce simultaneously the $V_{int}(V_{ext})$ curves (Fig. 4), the $R_S(V_{ext})$ (Fig. 5a), the $R_S(V_{int})$ (Fig. 5b), as well as the external $J(V_{ext})$ and internal current vs. voltage $J(V_{int})$ curves, as shown in Fig. 6.

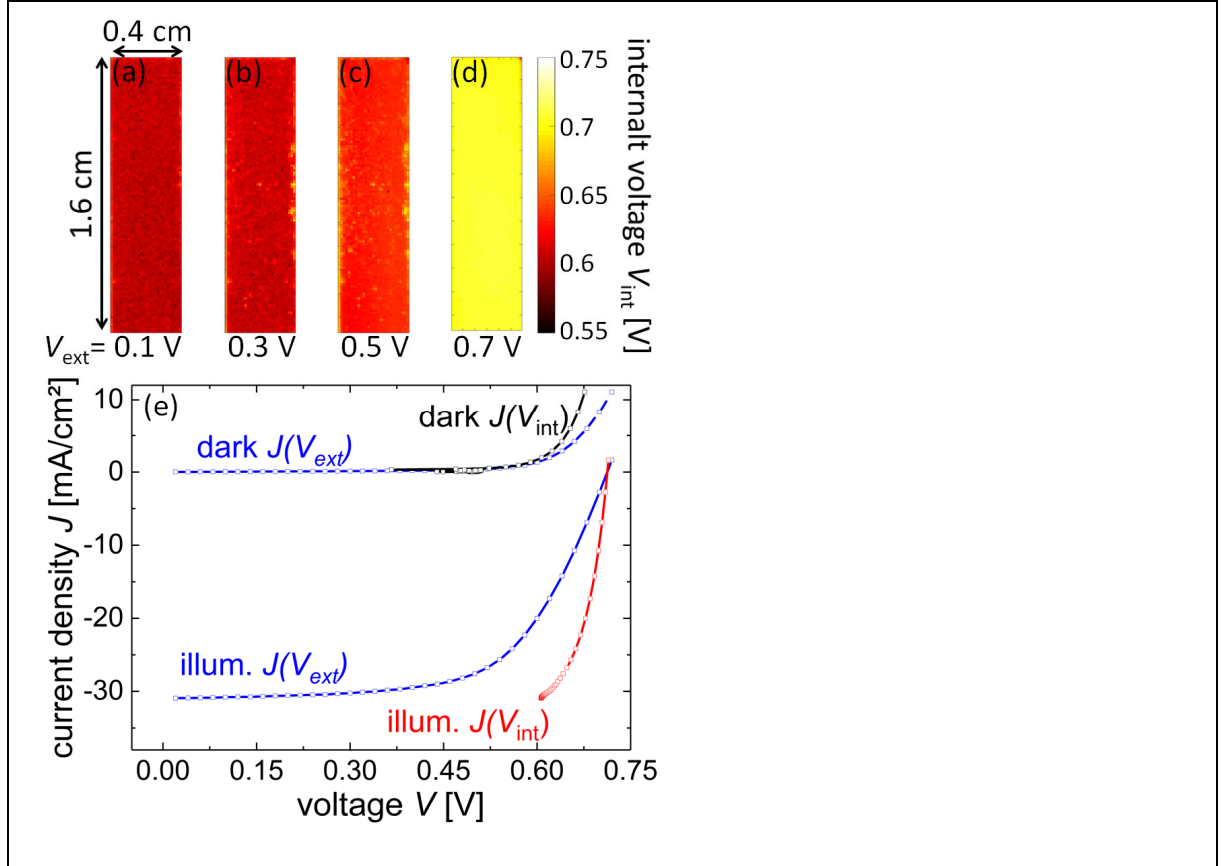


Fig. 3: (a)-(d) Experimentally determined internal voltage maps at various external voltages calculated from luminescence images under illumination. It is visible that even at low external voltages, still a significant amount of luminescence is seen which shows a large internal voltage. The sample looks homogenous which allows the use of the average across the sample. (e) J/V and J/V_{int} characteristics which are determined simultaneously by taking luminescence images during the J/V sweep once in the dark and once under illumination. The internal voltages are larger than the external voltages when the current is negative and vice versa. Especially at short circuit under illumination the internal voltage is much larger than the external voltage.

Note that in the case $J_L \gg J_B \gg J_0$ the residual short circuit internal voltage given in

Eq. (10) reduces to

$$V_{int}^{SC} \approx \frac{kT}{q} \log\left(\frac{J_L}{J_B}\right). \quad (16)$$

This approximation is valid also for the non-ideal recombination situation ($n_{id} \neq 1$) as shown in the supplementary information. With Eq. (16), J_B is essentially fixed by the experimental value of V_{int}^{SC} for the semi-analytical approach using Eq. (8). We use $J_B = 2.5 \times 10^{-9} \text{ mAcm}^{-2}$ to reproduce an asymptotic value $V_{int}^{SC} \approx 604 \text{ mV}$ as shown in Fig. 4. A good simultaneous fit of the illuminated and dark JV characteristics (as shown in Fig. 6) requires an ideality factor $n_{id} = 1.3$. The saturation current density J_0 is adjusted to yield the experimental open circuit voltage $V_{OC} = 710 \text{ mV}$ with a photo-generated current density $J_L = 32.5 \text{ mAcm}^{-2}$. Note that the measured short circuit current is reduced by

$$\Delta J_{SC} = J_L - J_{SC} \approx J_0 \left(\frac{J_L}{J_B} \right)^{\frac{1}{n_{id}}}. \quad (17)$$

The approximate value is obtained from Eq. (11) for $J_L \gg J_B \gg J_0$. In the supplementary information we show that Eq (17) is also a good approximation for $n_{id} \neq 1$. Finally an external series resistance $R_{ext} = 3.5 \text{ } \Omega\text{cm}^2$ is added such that the total series resistance adds up to $R_S = R_B + R_{ext}$ where R_S denotes the *experimental* value from Eq. (15) and R_B the *theoretical* value from Eq. (12). Note that this relatively high value of the external series resistance R_{ext} is on the one hand due to the relatively low conductivity of the ZnO window layer in industrial solar cells and on the other hand to the experimental contacting scheme used in this work.

With these assumptions, we can reproduce the overall behavior of the $R_S(V_{ext})$ and $R_S(V_{int})$ curves in Fig. 5, the $V_{int}(V_{ext})$ curve shown in Fig. 4, as well as the external and internal current vs. voltage curves in Fig. 6. For completeness, we have also included the simpler dependency of the internal series resistance R_{int} on the internal voltage V_{int} according to Refs. [23,24] as expressed by Eq. (13) and will refer to this approach to as the *pin*-model, in contrast to the *pn*-model as given by Breitenstein [25,26] and derived in section II.

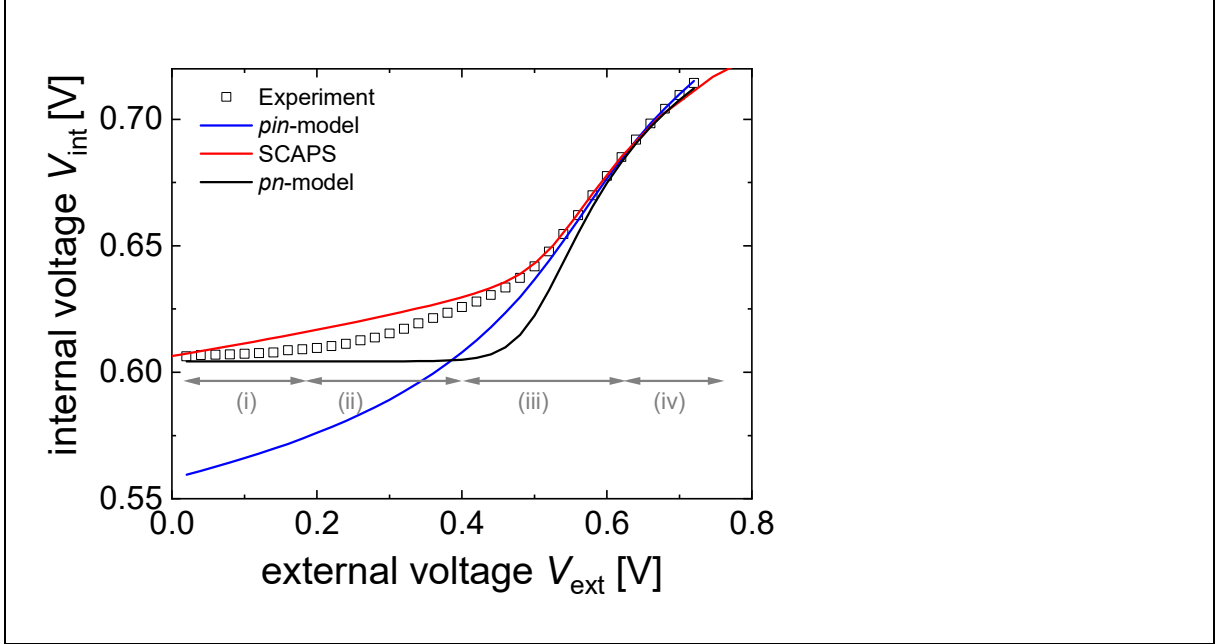
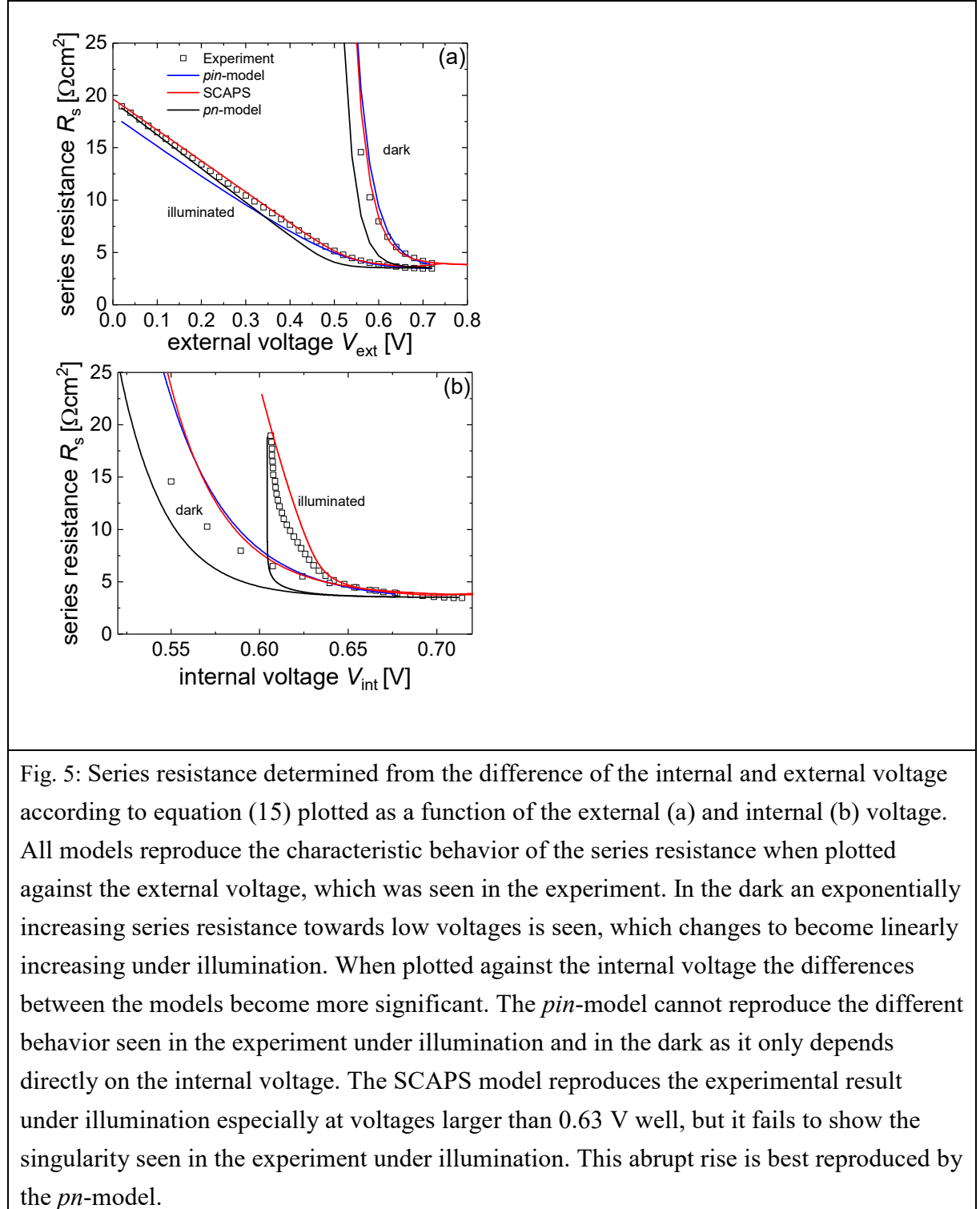


Fig. 4: Internal voltages V_{int} as determined from luminescence images via Eq. (14) as a function of the externally applied voltage V_{ext} (open symbols). The full red line corresponds to numerical simulations via SCAPS using the parameter set given in the supplementary information. The black line is obtained from the pn -model described in sect. II using $J_B = 2.5 \times 10^{-9} \text{ mAcm}^{-2}$, $J_0 = 2.45 \times 10^{-8} \text{ mAcm}^{-2}$, $J_L = 32.5 \text{ mAcm}^{-2}$, $n_{\text{id}} = 1.3$ and $R_{\text{ext}} = 3.5 \text{ } \Omega\text{cm}^2$. The blue line represents the pin -model [Eq. (13)] with $R_0 = 6.9 \times 10^7 \text{ } \Omega\text{cm}^2$ and $R_{\text{ext}} = 3.26 \text{ } \Omega\text{cm}^2$. The voltage ranges (i)-(iv) represent (i) a saturation at a constant value of the experimental V_{int} values at $V_{\text{int}} \approx V_{\text{int}}^{\text{SC}}$ towards lower voltages [$0 \leq V_{\text{ext}} < 0.2V$], (ii) a slight leveling-off in the range $0.2V \leq V_{\text{ext}} \leq 0.5V$, (iii) a steep increase of V_{int} for $0.5V \leq V_{\text{ext}} \leq 0.65V$, and (iv) a bending over in the range $0.65V \leq V_{\text{ext}}$ due to the external series resistance.

Within the SCAPS simulations, the internal voltage V_{int} is determined from the product of the electron and hole densities and calibrated by the external voltage at open circuit conditions, in analogy to the experiment. For the adaption of parameters within the numerical device simulations, we have to bear in mind that in Eq. (7), we have the proportionality $J_B \propto \sigma_{n0} / L_D \propto \mu_n / \sqrt{N_A}$. Thus, a lowering of J_B and the consequent increase of $V_{\text{int}}^{\text{SC}}$ results both, from reducing μ_n as well as from increasing N_A . Thus, to fit the experimental results,

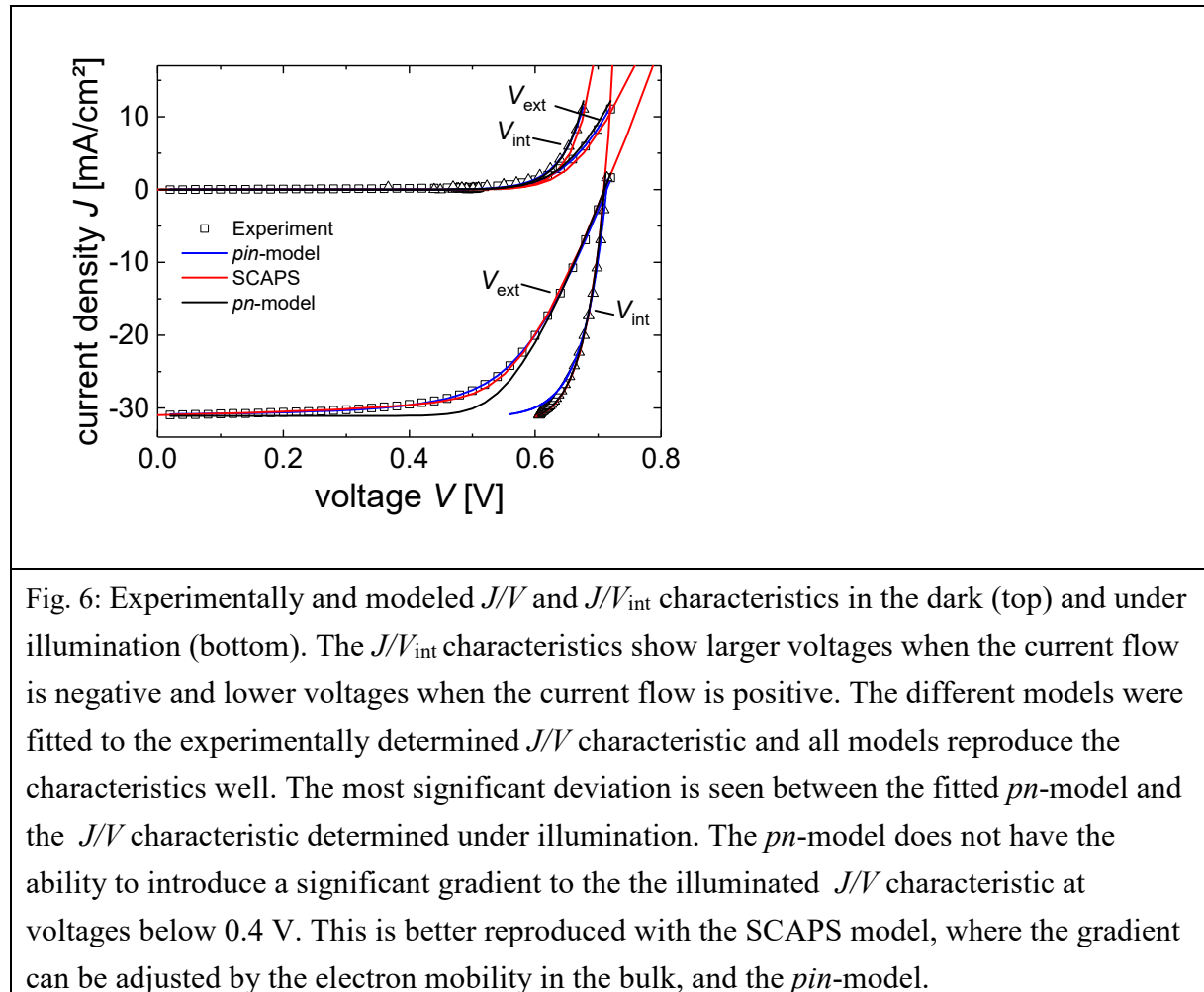
the doping and the electron mobility was manually adjusted to be able to reproduce on the one hand the dependence of the internal voltage on the external voltage (by lowering the doping density to $N_A = 2.1 \times 10^{15} \text{ cm}^{-3}$) and, on the other hand, the current vs. external voltage at low voltages under illumination (by lowering the electron mobility to $\mu_n = 3 \text{ cm}^2/\text{Vs}$). In the end the illumination intensity had to be adjusted slightly to 540 W/m^2 to fit the short circuit current of JV -characteristic. The final fit is shown in Fig. 6 together with the experimental results. The other parameters were kept equal to the one in Table 1 (supplementary information).

The relatively low value for the electron mobility ($\mu_n = 3 \text{ cm}^2/\text{Vs}$) is most likely a result of band gap fluctuations or potential fluctuations [39] in the Cu(In,Ga)Se₂ absorber. On the one hand, there is increasing experimental evidence for these fluctuations.[40,41,42] On the other hand, such fluctuations provide internal barriers for the transport of both types of carriers.[39] Thus, especially the (effective) minority carrier mobility may considerably fluctuate across the absorber on length scales that are not resolved by the present luminescence measurements. Because of the non-linear dependence of our measurements on μ_n as given by Eq. (17), the observed behavior could be over-proportionally determined by effective low mobility regions.



In the following, we will discuss the predictions of two models (*pn* and *pin*) and the result of the numerical device simulation in comparison to the experimental result. Figure 4

demonstrates that the SCAPS simulation (red line) reproduces most details of the experimental result (open symbols): (i) a saturation of $V_{\text{int}} \approx V_{\text{int}}^{\text{SC}}$ towards $V_{\text{ext}} = 0 \text{ V}$, (ii) a slight increase of V_{int} in the range $0.2 \text{ V} \leq V_{\text{ext}} \leq 0.5 \text{ V}$, (iii) a steep increase for $0.5 \text{ V} \leq V_{\text{ext}} \leq 0.65 \text{ V}$, and finally (iv) a bending over in the range $0.65 \text{ V} \leq V_{\text{ext}}$. Three of these four features are also reproduced by the *pn*-model (black line) only the transition between the low voltage saturation (i) and the steep increase (iii) is rather abrupt, essentially leaving out the transition regime (ii). Notably, the experimental curve in the saturation region (i) is even better reproduced by the analytical model as compared to the SCAPS simulations. The *pin*-model accurately reproduces the high voltage regions (iii) and (iv) but fails entirely to describe the saturation and finite internal voltages towards lower external voltages.



The dependency of the series resistance on the external voltage V_{ext} (Fig. 5a) is well described by all three approaches, the *pn*- and the *pin*-model as well as by the numerical simulations. All approaches yield a significant difference between the series resistance in the dark and under illumination, where R_S saturates at approximately the value of the external series resistance $R_{\text{ext}} = 3.5 \Omega\text{cm}^2$ for high voltages.

A much steeper increase of R_S in the dark towards lower voltages as compared to the increase of R_S under illumination is reproduced by all theoretical approaches. However, a more selective representation of the same data is the dependence of R_S on the *internal* voltage V_{int} (Fig. 5b). Here, the *pin*-model because of its direct functional dependence of R_{int} on V_{int} as given in Eq. (13) fails to reproduce any difference between the dark and the illuminated values. The *pn*-model fits the experimental data well except for the range from $0.61V \leq V_{\text{int}} \leq 0.64V$ which corresponds to the transition range (ii) in Fig. 4 whereas the singularity of R_S at $V_{\text{int}} \approx V_{\text{int}}^{\text{SC}} \approx 604 \text{ mV}$ is even better reproduced than by the SCAPS simulations.

C. Photocurrent collection efficiency

A voltage dependent series resistance as given in Eqs. (12) or (13) destroys basic relations that are derived from extrapolating the principle of detailed balance from the near equilibrium. The network theorem of Wong and Green [27] relates a differential modification dV_j of the junction voltage that results from a modification dV_{ext} of the terminal voltage with the differential photocurrent collection efficiency via

$$\frac{dV_{\text{int}}}{dV_{\text{ext}}} = f_c^{\text{ph}} := -\frac{dJ}{dJ_{\text{ph}}} . \quad (18)$$

In Eq. (18), the quantity dJ is the modification of the terminal current caused by a modification dJ_{ph} of the photocurrent and the derivative defines the photocurrent collection efficiency f_c^{ph} .

The standard application of the network theorem uses the fact that the local quantity $dV_j(x, y)$ is accessible as a function of the cell surface coordinates x, y by electro-modulated luminescence images. The validity of Eq. (18) then allows to determine the spatially resolved photocurrent collection efficiency $f_c^{ph}(x, y)$ from luminescence images [28,29,30,31,32].

The equivalent circuit model shown in Fig. 2b is a simple zero-dimensional model such we can replace J_{ph} by the light generated circuit current density J_L and the junction voltage by V_{int} . As shown in the supplementary information, analysis of a voltage bias dependent series resistance $R_S(V_{int})$ yields

$$\frac{dV_{int}}{dV_{ext}} = \frac{1}{1 + R_S \frac{dJ}{dV_{int}} + J \frac{dR_S}{dV_{int}}}. \quad (19)$$

For the photocurrent collection efficiency we find

$$f_c^{ph} := -\frac{dJ}{dJ_L} = \frac{1 + J \frac{dR_S}{dV_{int}}}{1 + R_S \frac{dJ}{dV_{int}} + J \frac{dR_S}{dV_{int}}}. \quad (20)$$

Comparison of Eqs. (19) and (20) shows that the network theorem of Wong and Green [27] only holds with either $dR_S/dV_{int} = 0$, i.e. in the absence of a bias dependence of R_S corresponding to the idea of a linear network, or at zero current bias. Note that the latter limit ($J \rightarrow 0$) ensures that the theorem is valid close to thermal equilibrium as required by the principle of detailed balance.

Figure 7 demonstrates the difference between dV_{int}/dV_{ext} and dJ/dJ_{sc} . When determining experimentally or with the SCAPS model the differential photocurrent collection efficiency via luminescence images and dV_{int}/dV_{ext} a decrease is seen towards lower voltages. This decrease is not seen when determining dJ/dJ_{sc} directly using a small short circuit current change (illumination change) within the SCAPS Simulations. The decrease seen for dV_{int}/dV_{ext} at low voltages under illumination results from the missing positive term $J dR_S/dV_{int}$ in Eq. (19) (J and dR_S/dV_{int} are both negative). Furthermore, it is seen in Fig. 7 that the experimentally

determined total photocurrent collection efficiency J/J_L , which is also well reproduced by the SCAPS simulations, does not show a decrease of towards lower voltages which emphasizes that Eq. 18 leads to erroneous results for the present samples.

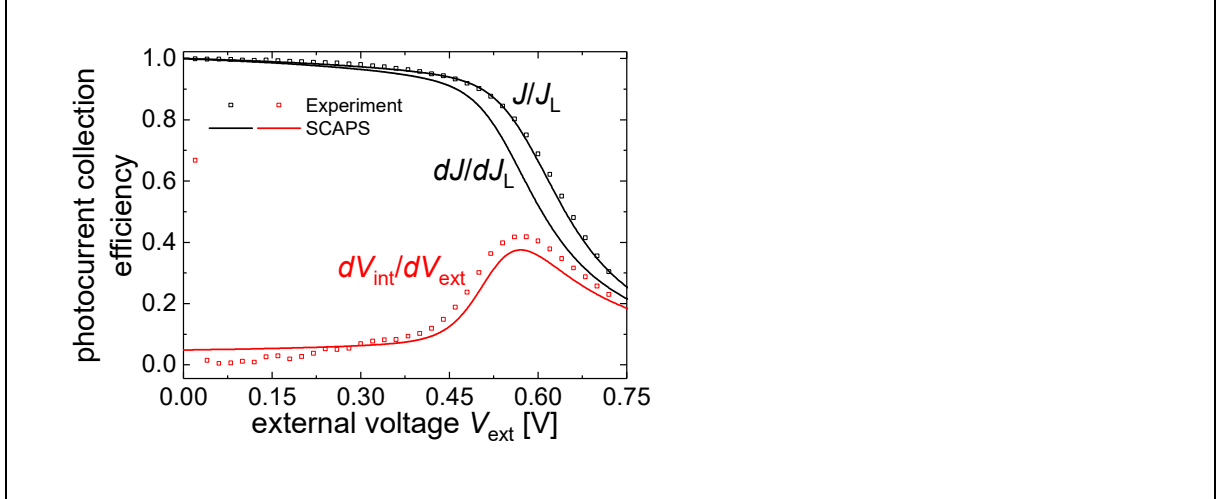


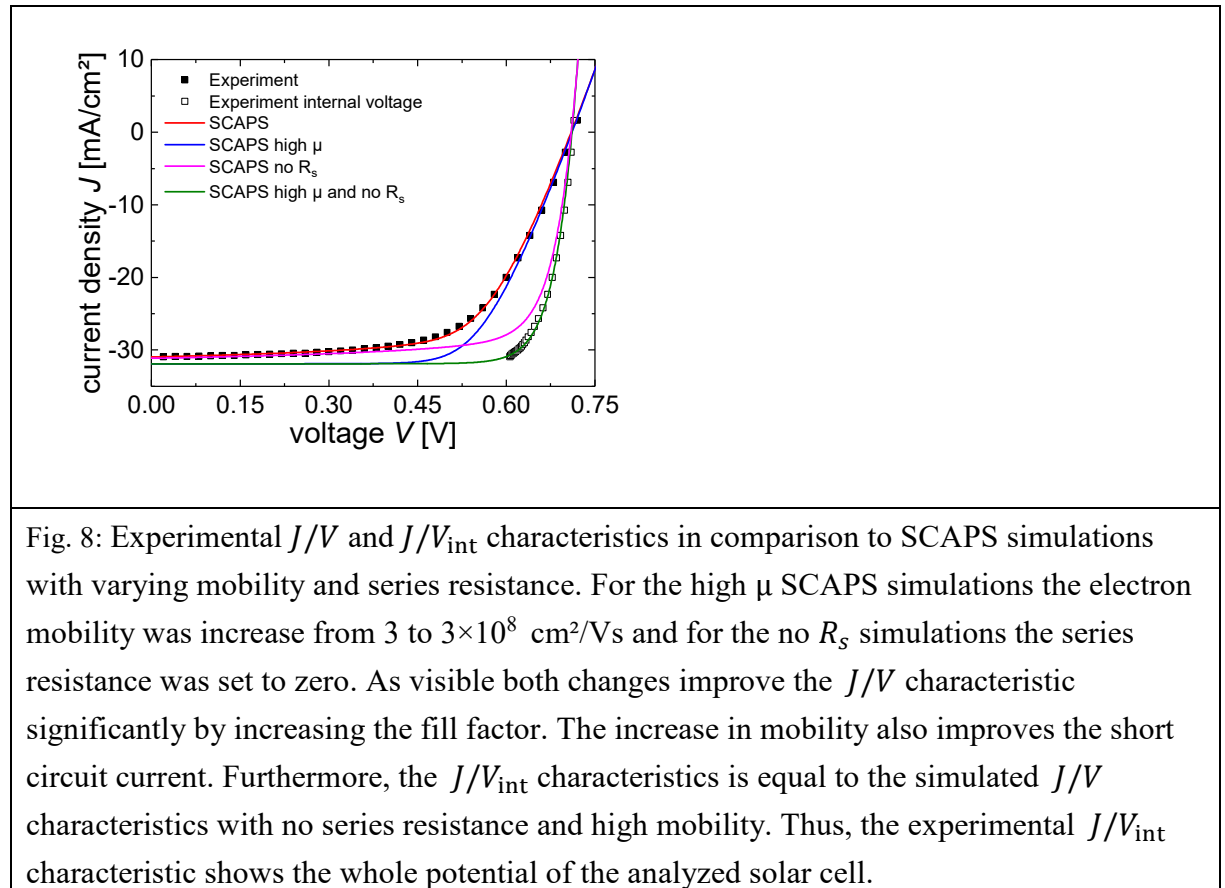
Fig. 7: Comparison of the two methods to determine the photocurrent collection efficiency. The results were found to be different in the experiment as well as the SCAPS simulations, which is in contrast to the network theorem of Wong and Green (Eq. 18). The photocurrent collection efficiency determined from the internal voltage is lower than the real photocurrent collection efficiency determined directly from artificially created photocurrent changes and decreases towards lower voltages. The difference is explained by a voltage dependent series resistance, which plays a major role for the analyzed Cu(In,Ga)Se₂ samples (Eq. 19 and 20).

D. Loss Analysis

Our numerical simulations and the modeling have explained all measured data, JV -curves and luminescence, by losses due to external and internal resistive effects. As a proof of concept we may remove these resistive effects from the simulations by reducing the external series resistance R_{ext} to zero and/or by increasing the electron mobility μ_n to a very high number ($\mu_n = 3 \times 10^8 \text{ cm}^2(\text{Vs})^{-1}$), whereas keeping all other parameters constant. Figure 8 visualizes the resulting JV -curves starting with the measured data and their simulation as already shown in

Fig. 6. As expected, changing R_{ext} from $3.5 \Omega\text{cm}^2$ to 0 yields a substantial improvement of the fill factor leaving V_{OC} and J_{SC} unchanged. On the other hand, the change from $\mu_n = 3 \text{ cm}^2(\text{Vs})^{-1}$ to $3 \times 10^8 \text{ cm}^2(\text{Vs})^{-1}$ (keeping R_{ext} at $3.5 \Omega\text{cm}^2$), enhances J_{SC} from 31.1 mAcm^{-2} to 31.9 mAcm^{-2} .

Finally, using both changes at the same time yields a greatly improved JV -characteristics that in addition fits the experimentally determined (internal) J/V_{int} -curve. The latter point highlights the consistency of our approach and proofs that J/V_{int} -curves determined from luminescence measurements are suitable to determine loss-free current-voltage curves and to determine the implied efficiency potential of a solar cell.



In order to evaluate the power losses due to external and internal resistance more closely, we plot the data from Fig. 8 in the form of power vs. voltage curves by multiplying the currents

with the respective voltages. Note that the efficiency axis on the right of Fig. 9 is obtained by scaling the measured output power by the ratio $J_{SC}^{PLsetup} / J_{SC}^{AM1.5} = 31.0 \text{ mAcm}^{-2} / 29.2 \text{ mAcm}^{-2} = 1.06$ of short circuit current measured during the luminescence measurement in the sun simulator and that measured in the sun simulator. With this correction, we have an efficiency of $\eta = 13.4 \%$ (with a fill factor of $FF = 64 \%$) for the experimental data as well as for the SCAPS simulations, an efficiency of $\eta_{\mu} = 14.6 \%$ for the simulated high mobility data, $\eta_R = 15.8 \%$ for the case without external Ohmic series resistance, and $\eta_{\mu R} = 17.6 \%$ ($FF = 76 \%$) for high mobility *and* zero series resistance. Thus, the loss due to the internal series resistance amounts to $\Delta\eta_{\mu} = \eta_{\mu} - \eta = 1.2 \%$ and that of the external series resistance $\Delta\eta_R = \eta_R - \eta = 2.4 \%$. The overall difference $\Delta\eta_{\mu R} = \eta_{\mu R} - \eta_{exp} = 4.2 \%$ between the standard model and the loss-free output efficiency contains an additional mixed term of 0.6% that results from the combined consequences of external and internal series resistance. Also shown in Fig. 9 is the fact that the simulated loss-free power curve fits the experimental internal power curve $P_{int} = JV_{int}$ (open squares) as well as the internal power curve obtained from simulations (crosses).

A further consistency check is given by comparing the measured ratio between the luminescence Φ_{SC} under short circuit current and Φ_{OC} under open circuit with the ratio $\Delta J_{SC} / J_L$. Here, the difference $\Delta J_{SC} = J_L - J_{SC}$ denotes the total loss of short circuit current with respect to the total photogenerated current J_L . For the general case, including ideality factors $n_{id} \neq 1$, we find

$$\frac{\Phi_{SC}}{\Phi_{OC}} = \left(\frac{\Delta J_{SC}}{J_L} \right)^{n_{id}}. \quad (21)$$

As shown in the supplementary information, Eq. (21) follows from Eq. (11) for the case $n_{id} = 1$ and from the approximate Eqs. (16) and (17). The luminescence ratio in our experiment is $\Phi_{SC} / \Phi_{OC} \approx 1.7 \%$ whereas in the simulation of our experiment, we have $\Delta J_{SC} = 1.4 \text{ mAcm}^{-2}$

based on a total photogenerated current $J_L = 32.5 \text{ mAcm}^{-2}$ and a measured short circuit current $J_{SC} = 31.1 \text{ mAcm}^{-2}$. With an ideality factor $n_{id} = 1.3$ we have $(\Delta J_{SC} / J_L)^{n_{id}} = (0.043)^{1.3} = 0.0167$ in good agreement with the measured luminescence ratio.

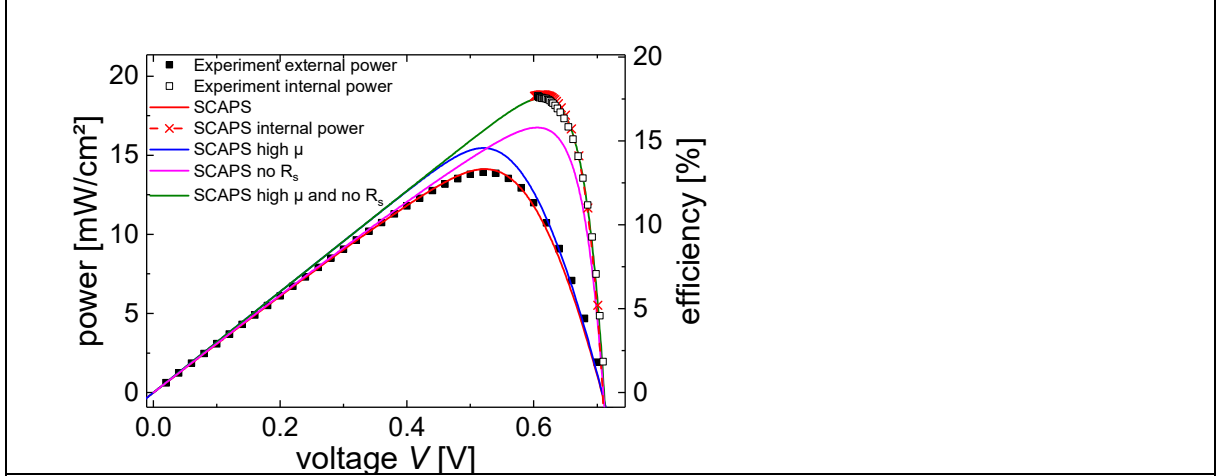


Fig. 9: Experimental power characteristics determined from the J/V and J/V_{int} characteristics in comparison to SCAPS simulations with varying mobility and series resistance. The power curve determined using the internal voltage is noted as internal power. For the high μ SCAPS simulations the electron mobility was increased from 3 to $3 \times 10^8 \text{ cm}^2/\text{Vs}$ and for the no R_s simulations the series resistance was set to zero. The increase in the mobility results in an efficiency increase of absolute 1.2 %, the decrease in the series resistance results in an increase of absolute 2.4 %, while an improvement of both parameters improves the efficiency by absolute 4.2 %, which surpasses the sum of the individual improvements.

IV. Conclusions

The present investigations have highlighted the value of combined electrical and luminescence measurements under light and voltage bias for the determination of internal as well as external resistive losses in solar cells. For the specific case of Cu(In,Ga)Se_2 solar cells we have found a significant residual luminescence under short circuit conditions indicating the presence of photo-generated electron-hole pairs that are not collected by the junction. This finding also implies that the internal voltage, defined as the split between the quasi-Fermi-levels of electrons and holes, significantly differs from the external voltage at the terminals of the device. We attribute this effect to the presence of an internal series resistance, due to the

transport of electrons through the space charge region of the Cu(In,Ga)Se₂ absorber layer. We have developed a detailed theoretical model for this effect and have used this model, complemented by numerical simulations, to analyze the incomplete collection of photo-generated free charge carriers in the Cu(In,Ga)Se₂ the solar cell and to identify the specific losses arising as a consequence of the internal and the external series resistance.

From our experiments and our theoretical considerations, we conclude that residual short circuit luminescence is not only significant for crystalline silicon solar cells with a thickness of hundreds of μm and a corresponding slow diffusion of charge carriers [12,13,14] but for any photovoltaic device. This is because the residual luminescence is a direct measure for the free energy loss that occurs during charge carrier collection within any solar cell.[43] Since a finite gradient of the electrochemical potential is always necessary for the transport of charge carriers and because any split of the electrochemical potentials *must* cause externally measurable luminescence, this free energy loss should be measurable in any solar cell.

One might further look at the respective role of internal and external resistive losses as discussed here in terms of the charge carrier separation and contact selectivity of solar cells. [44] The internal series resistance results from a *difference in electrochemical potential* corresponding to a kinetic loss as described in the selectivity/recombination model of Roe and coworkers.[45] In contrast, the external resistance results from a *difference in electrical potential* and hence is a true Ohmic resistance, as used in the contact selectivity concept of Brendel and Peibst. [46] From the present work, we conclude that both effects are present in real devices, kinetic (internal) limitations at low or zero external voltages, Ohmic (external) limitations at higher voltages. Finally, we have shown experimentally and theoretically that residual short circuit luminescence leads to a violation of a basic network theorem [27] for the carrier collection in solar cells whereas the superposition of short circuit luminescence and electroluminescence [15] is still valid.

In summary, the residual short-circuit luminescence that we describe here theoretically and experimentally should be a rather general feature of solar cells and the methodology developed should prove itself useful for a wide variety of other devices.

Acknowledgements

The authors are grateful to A. Gerber and T. Kirchartz for collaboration and discussions. This work has been partially supported by the Bundesministerium für Wirtschaft und Energie (BMWi) under contract 0324297 and under contract 0324353.

References

- 1 J. Mattheis, J. H. Werner, and U. Rau, Finite mobility effects on the radiative efficiency limit of pn-junction solar cells, *Phys. Rev. B* **77**, 085203 (2008).
- 2 W. Shockley and H. J. Queisser, Detailed balance limit of efficiency of p-n-junction solar cells, *J. Appl. Phys.* **32**, 510 (1961).
- 3 T. Fuyuki, H. Kondo, T. Yamazaki, Y. Takahashi, and Y. Uraoka, Photographic surveying of minority carrier diffusion length in polycrystalline silicon solar cells by electroluminescence, *Appl. Phys. Lett.* **86**, 262108 (2005).
- 4 T. Trupke, R. A. Bardos, M. C. Schubert, and W. Warta, Photoluminescence imaging of silicon wafers, *Appl. Phys. Lett.* **89**, 044107 (2006).
- 5 K. Bothe and D. Hinken, Quantitative luminescence characterization of crystalline silicon solar cells, in *Semiconductors and Semimetals Vol. 89, Advances in Photovoltaics Vol. 2*, edited by G. P. Willeke and E. R. Weber (Academic Press, Burlington, 2013), pp. 259-339.
- 6 T. Kirchartz, A. Helbig, B. E. Pieters, and U. Rau, Electroluminescence analysis of thin-film solar modules, in *Advanced Characterization Techniques for Thin Film Solar Cells, 2nd ed.* edited by D. Abou-Ras, T. Kirchartz, and U. Rau (Wiley-VCH, Weinheim, Germany, 2016), pp. 61–80.
- 7 A. Gerber, V. Huhn, T. M. H. Tran, M. Siegloch, B. E. Pieters, and U. Rau, Advanced large area characterization of thin-film solar modules by electroluminescence and thermography imaging techniques, *Sol. Ener. Mat. Sol. Cells* **135**, 35 (2015).
- 8 O. Breitenstein, F. Frühauf, and J. Bauer, Advanced local characterization of silicon solar cells, *Phys. Status Solidi A* **214**, 1700611 (2017)
- 9 F. Babbe, L. Choubrac, and S. Siebentritt, The optical diode ideality factor enables fast screening of semiconductors for solar cells, *Sol. RRL* **2**, 1800248 (2018).
- 10 U. Rau, Reciprocity relation between photovoltaic quantum efficiency and electroluminescent emission of solar cells, *Phys. Rev. B* **76**, 085303 (2007).
- 11 P. Würfel, The chemical potential of radiation, *J. Phys. C, Solid State Phys.* **15**, 3967 (1982).
- 12 M.D. Abbott, R.A. Bardos, T. Trupke, K. Fisher, E. Pink, The effect of diffusion-limited lifetime on implied current voltage curves based on photoluminescence data, *J. Appl. Phys.* **102**, 044502 (2007)
- 13 D. Hinken, K. Bothe, K. Ramspeck, S. Herlufsen, and R. Brendel, Determination of the effective diffusion length of silicon solar cells from photoluminescence, *J. Appl. Phys.* **105**, 104516 (2009).
- 14 M. K. Juhl and T. Trupke, The impact of voltage independent carriers on implied voltage measurements on silicon devices, *J. Appl. Phys.* **120**, 165702 (2016).

- 15 U. Rau, IEEE J. Photovoltaics **2**, 169 (2012).
- 16 T. Trupke, E. Pink, R. A. Bardos, and M. D. Abbott, Spatially resolved series resistance of silicon solar cells obtained from luminescence imaging, Appl. Phys. Lett. **90**, 093506 (2007).
- 17 D. Hinken, K. Ramspeck, K. Bothe, B. Fischer, and R. Brendel, Series resistance imaging of solar cells by voltage dependent electroluminescence, Appl. Phys. Lett. **91**, 182104 (2007).
- 18 O. Breitenstein, J. Bauer, D. Hinken, and K. Bothe, The reliability of thermography- and luminescence-based series resistance and saturation current density imaging, Sol. Ener. Mat. Sol. Cells **137**, 50 (2015)
- 19 A. Helbig, T. Kirchartz, R. Schaeffler, J. H. Werner, and U. Rau, Quantitative electroluminescence analysis of resistive losses in Cu(In, Ga)Se₂ thin-film modules, Sol. Ener. Mat. Sol. Cells **94**, 979 (2010)
- 20 M. Paire, L. Lombez, J.-F. Guillemoles, and D. Lincot, Measuring sheet resistance of CIGS solar cell's window layer by spatially resolved electroluminescence imaging, Thin Solid Films **519**, 7493 (2011)
- 21 T. M. H. Tran, B. E. Pieters, C. Ulbrich, A. Gerber, T. Kirchartz, and U. Rau, Transient phenomena in Cu(In,Ga)Se₂ solar modules investigated by electroluminescence imaging, Thin Solid Films **535**, 307 (2013)
- 22 T. M. H. Tran, B. E. Pieters, M. Schneemann, T. C. M. Müller, A. Gerber, T. Kirchartz, and U. Rau, Quantitative evaluation method for electroluminescence images of a-Si: H thin-film solar modules, Phys. Stat. Sol. RRL **7**, 627 (2013)
- 23 T. C. M. Müller, B. E. Pieters, U. Rau, and T. Kirchartz, Analysis of the series resistance in pin-type thin-film silicon solar cells, J. Appl. Phys. **113** (2013)
- 24 U. Würfel, D. Neher, A. Spies, and S. Albrecht, Impact of charge transport on current-voltage characteristics and power-conversion efficiency of organic solar cells, Nat. Commun. **6**, 6951(2015).
- 25 O. Breitenstein, An alternative one-diode model for illuminated solar cells, IEEE J. Photov. **4**, 899 (2014)
- 26 O. Breitenstein, An alternative one-diode model for illuminated solar cells, Energy Procedia **55**, 30 (2014)
- 27 J. Wong and M. A. Green, From junction to terminal: Extended reciprocity relations in solar cell operation, Phys. Rev. B. **85**, 235205 (2012)
- 28 U. Rau, V. Huhn, L. Stoicescu, M. Schneemann, Y. Augarten, A. Gerber, and B. E. Pieters, Photocurrent collection efficiency mapping of a silicon solar cell by a differential luminescence imaging technique, Appl. Phys. Lett. **105**, 163507 (2014).

- 29 J. Wong, R. Sridharan, Y. C. Wang, and T. Mueller, Differential electroluminescence imaging and the current transport efficiency of silicon wafer solar cells, in IEEE 40th Photovoltaic Specialist Conference (PVSC), Denver, CO, 2014, p. 975.
- 30 A. Delamarre, L. Lombez, K. Watanabe, M. Sugiyama, Y. Nakano, and J. F. Guillemoles, Experimental demonstration of optically determined solar cell current transport efficiency map, IEEE J. Photovoltaics **6**, 528 (2016).
- 31 V. Huhn, A. Gerber, Y. Augarten, B. E. Pieters, and U. Rau, Analysis of Cu(In,Ga)Se₂ thin-film modules by electro-modulated luminescence, J. Appl. Phys. **119**, 095704 (2016).
- 32 V. Huhn, B. E. Pieters, Y. Augarten, A. Gerber, D. Hinken, and U. Rau, Imaging photocurrent collection losses in solar cells, Appl. Phys. Lett. **109**, 223502 (2016).
- 33 S. M. Sze and K. K. Ng, '*Physics of Semiconductor Devices*' (John Wiley and Sons, Hoboken, NJ, 2007) pp.85-91.
- 34 B. Dimmler and R. Wächter, Manufacturing and application of CIS solar modules, Thin Solid Films **515**, 5973 (2007)
- 35 M. Burgelman, P. Nollet, and S. Degraeve, Modelling polycrystalline semiconductor solar cells, Thin Solid Films, **361-362**, 527 (2000).
- 36 J. F. L. Salas, S. J. Heise, M. Richter, V. Gerliz, M. S. Hammer, J. Ohland, I. Hammer-Riedel, Simulation of metastable changes in time resolved photoluminescence of Cu(In,Ga)Se₂ thin film solar cells upon light soaking treatment, Thin Solid Films **633**, 40 (2016)
- 37 S. J. Heise, V. Gerliz, M. S. Hammer, J. Ohland, J. Keller, and I. Hammer-Riedel, Light-induced changes in the minority carrier diffusion length of Cu(In,Ga)Se₂ absorber material, Sol. Ener. Mat. Sol. Cells **163**, 270 (2017).
- 38 T. Kirchartz, U. Rau, M. Hermle, A. W. Bett, A. Helbig, and J. H. Werner, Internal voltages in GaInP/GaInAs/Ge multijunction solar cells determined by electroluminescence measurements, Appl. Phys. Lett. **92**, 123502 (2008).
- 39 J. H. Werner, J. Mattheis, and U. Rau, Efficiency limitations of polycrystalline thin film solar cells: Case of Cu(In,Ga)Se₂, Thin Solid Films **480-481**, 399 (2005).
- 40 J. Mattheis, U. Rau, and J. H. Werner, Light absorption and emission in semiconductors with band gap fluctuations - A study on Cu(In,Ga)Se₂ thin films, J. Appl. Phys. **101**, 113519 (2007).
- 41 D. Abou-Ras, N. Schäfer, C. J. Hages, S. Levenko, J. Marquez, and T. Unold, Inhomogeneities in Cu(In,Ga)Se₂ thin films for solar cells: Band-gap versus potential fluctuations, Solar RRL **2**, 1700199 (2018).
- 42 J. P. Teixeira, P. M. P. Salomé, B. Alves, M. Edoff, and J. P. Leitão, Evidence of limiting effects of fluctuating potentials on V_{OC} of Cu(In,Ga)Se₂ thin-film solar cells, Phys. Rev. Appl. **11**, 054013.

- 43 R. Brendel, S. Dreissigacker, N.-P. Harder, and P. P. Altermatt, Theory of analyzing free energy losses in solar cells, *Appl. Phys. Lett.* **93**, 173503 (2008).
- 44 U. Rau and T. Kirchartz, Charge carrier collection and contact selectivity in solar cells, *Adv. Mat. Interf.* **6**, 1900252 (2019).
- 45 E. T. Roe, K. E. Egelhofer, and M. C. Lonergan, Limits of contact selectivity/recombination on the open-circuit voltage of a photovoltaic, *ACS Appl. Energy Mater.* **1**, 1037 (2018).
- 46 R. Brendel and R. Peibst, Contact selectivity and efficiency in crystalline silicon photovoltaics, *IEEE J. Photov.* **6**, 1413 (2016).